Gate-compatible circuit quantum electrodynamics in a three-dimensional cavity architecture

Zezhou Xia,[1,†] Jierong Huo,[1,†] Zonglin Li,[1,†] Jianghua Ying,[2,†] Yulong Liu,[3,†] Xin-Yi Tang,[1] Yuqing Wang,[3] Mo Chen,[3] Dong Pan,[4] Shan Zhang,[1] Qichun Liu,[3] Tiefu Li,[5,3] Lin Li,[3] Ke He,[1,3,6,7] Jianhua Zhao,[4] Runan Shang,[3,7] and Hao Zhang[1,3,6,*]

[1] *State Key Laboratory of Low Dimensional Quantum Physics, Department of Physics, Tsinghua University, Beijing 100084, China*

[2] *Yangtze Delta Region Industrial Innovation Center of Quantum and Information, Suzhou 215133, China*

[3] *Beijing Academy of Quantum Information Sciences, Beijing 100193, China*

[4] *State Key Laboratory of Superlattices and Microstructures, Institute of Semiconductors, Chinese Academy of Sciences, P.O. Box 912, Beijing 100083, China*

[5] *School of Integrated Circuits and Frontier Science Center for Quantum Information, Tsinghua University, Beijing 100084, China*

[6] *Frontier Science Center for Quantum Information, Beijing 100084, China*

[7] *Hefei National Laboratory, Hefei 230088, China*

(Received 13 November 2023; revised 4 December 2023; accepted 21 February 2024; published 18 March 2024)

Semiconductor-based superconducting qubits offer a versatile platform for studying hybrid quantum devices in circuit quantum electrodynamics (QED) architecture. Most of these circuit QED experiments utilize coplanar waveguides, where the incorporation of dc gate lines is straightforward. Here, we present a technique for probing gate-tunable hybrid devices using a three-dimensional (3D) microwave cavity. A recess is machined inside the cavity wall for the placement of devices and gate lines. We validate this design using a hybrid device based on an InAs-Al nanowire Josephson junction. The coupling between the device and the cavity is facilitated by a long superconducting strip, the antenna. The Josephson junction and the antenna together form a gatemon qubit. We further demonstrate the gate-tunable cavity shift and two-tone qubit spectroscopy. This technique could be used to probe various quantum devices and materials in a 3D circuit QED architecture that requires dc gate voltages.

DOI: 10.1103/PhysRevApplied.21.034031

I. INTRODUCTION

Superconducting circuits based on Josephson junctions play a crucial role in solid-state quantum information processing [1]. By replacing the insulating barrier (Al_2O_3) in the Josephson element with a semiconductor, new types of qubits, such as gatemons, 0-π qubits, and Andreev qubits, can be realized [2–14]. In addition, circuit quantum electrodynamics (QED) provides an approach to exploring the fascinating physics of semiconductor-superconductor hybrids at microwave frequencies [15–24]. These hybrid devices are predicted to exhibit exotic phases of matter, including topological superconductivity [25,26]. While transport measurements have been the primary approach to studying these states [27–30], proposals based on their microwave responses offer an additional experimental tool that allows for fast control and readout [31–34].

Previous circuit QED experiments on these hybrid devices were conducted using a two-dimensional (2D) architecture with superconducting coplanar waveguides [35]. The incorporation of a dc gate line, which is essential for hybrid devices, is simple in the 2D architecture. To ensure compatibility with an in-plane magnetic field, the superconducting film of the waveguide was often designed to be thin with high-density artificial holes for vortex pinning [36–39]. However, a magnetic field perpendicular to the substrate can still significantly degrade the performance of the resonator [37]. An alternative approach is the use of a three-dimensional (3D) cavity architecture [40]. Incorporating hybrid devices with dc gate lines into a 3D cavity presents considerable challenges. Previous attempts have utilized either a superconducting electrode inserted into the cavity or the cavity itself to apply a dc bias [41,42]. These approaches yield very weak electric fields compared to on-chip gate electrodes for hybrid devices. Directly inserting the device chip with on-chip gate electrodes into a 3D cavity can, however, deteriorate the cavity quality substantially [43].

*hzquantum@mail.tsinghua.edu.cn

†These authors contributed equally to this work.

In this paper, we present a 3D cavity architecture that is compatible with a dc gate electrode for probing hybrid devices. For resilience to magnetic fields, we utilized a copper cavity [44–46]. The ohmic dissipation caused by copper should not be an issue, given that acceptable coherence times (∼ 0.1 ms) have been reported in copper-cavity-based superconducting qubits [47]. Moreover, the strong thermal anchoring of copper helps in cooling the temperature of the cavity photons and the device chip. The architecture involves machining a recess by "digging a small room" on a sidewall of the cavity. The hybrid device, an InAs-Al nanowire Josephson junction, is placed inside this recess. This spatial separation between the device and the cavity can mitigate their direct coupling and minimize unwanted loss. A long superconducting strip, termed the antenna, couples the device to the cavity. The antenna and the InAs-Al nanowire together form a gatemon qubit. We validated this design by demonstrating a gate-tunable shift of the cavity resonance and the qubit spectroscopy. Our technique enables the probing of hybrid superconductor-semiconductor devices in a 3D circuit QED architecture where gate voltages and a magnetic field are desired.

II. CAVITY AND DEVICE DESIGN

Figure 1(a) shows a photograph of the cavity-device architecture, with the schematics illustrated in Figs. 1(b)–1(d). The major modification, in comparison to traditional 3D cavities, is a small recess machined on the cavity wall; see Fig. 1(d) for an enlarged view. The height of this recess is larger than the thickness of the

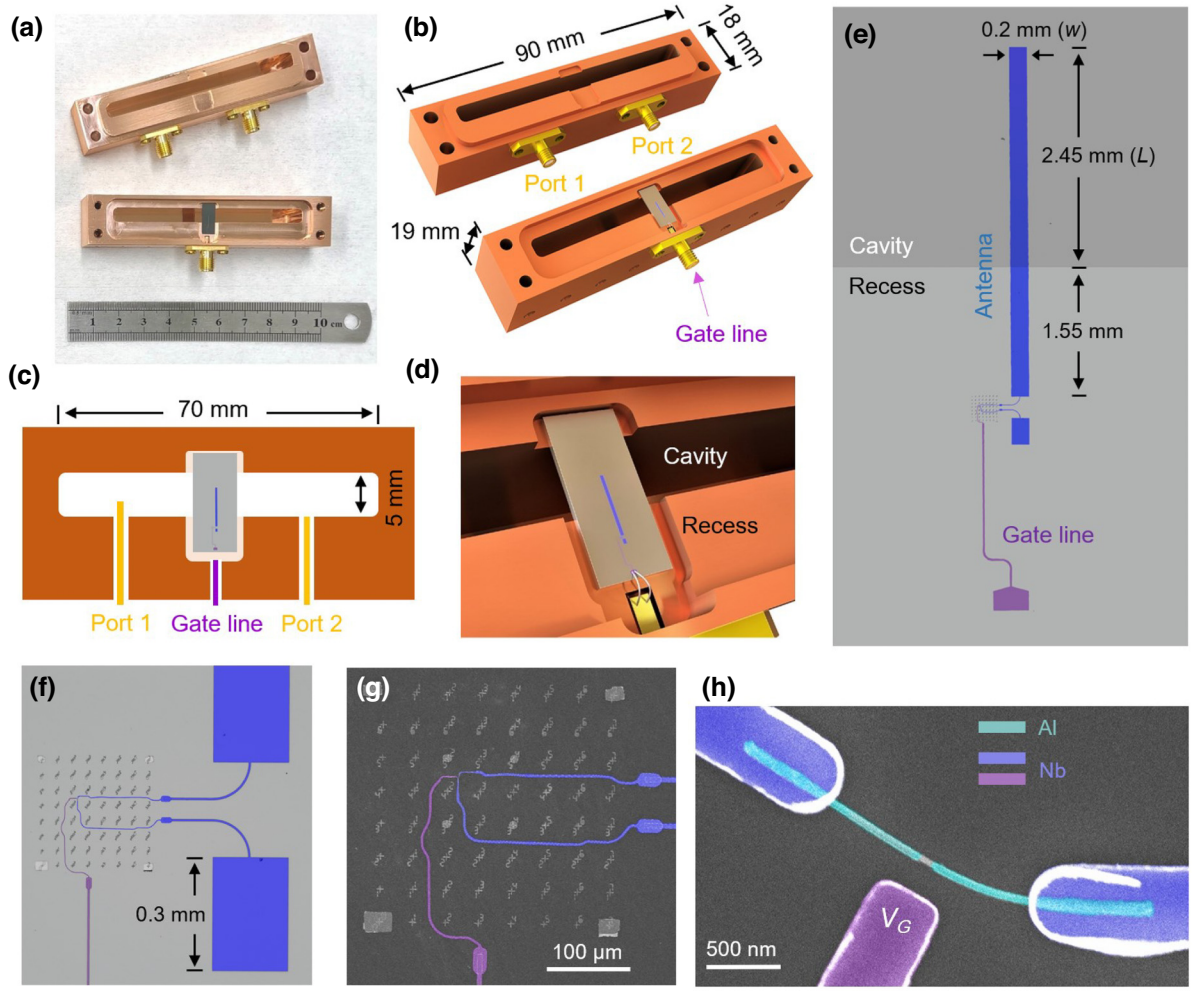

FIG. 1. Design of a gate-compatible 3D circuit QED architecture. (a) Photograph of a 3D copper cavity and a 10-cm-scale ruler. The upper half of the cavity has two commercial SubMiniature version A (SMA) connectors (ports 1 and 2) for signal coupling. The lower half has an SMA connector for the gate line. The device chip is in the recess machined within the cavity wall. (b) A 3D schematic of the design (not to scale). (c) A 2D schematic of the cavity midplane. (d) A schematic enlargement of the recess and the device chip. (e) Optical image of the device chip. The dark gray region is false-colored to highlight the cavity region, while the light gray is the part inside the recess. (f) An enlargement of the chip on the device part. (g),(h) Device SEMs (false colored).

device chip, ensuring that the chip can be inserted appropriately; see Fig. 5 in the Appendix for its cross-sectional schematic. Half of the device chip lies within the cavity, while the other half is inserted into the recess. Two SubMiniature version A (SMA) pins (labeled "Port 1" and "Port 2") penetrate the cavity, connecting the cavity modes to the measurement circuitry. In this work, we measured the reflection coefficient using only port 1, keeping the pin of port 2 grounded and not inserted into the cavity. A dc gate line connects to a third SMA pin, which is bonded onto the device chip. The device and the on-chip gate line are located inside the recess, spatially separated from the cavity. This separation helps to avoid direct coupling between the device region and cavity modes, minimizing unwanted dissipation and/or loss caused by the gate line and debris and/or residue from the device fabrication process. As shown in Fig. 1(c), the cavity size is as follows: 70 mm in length, 5 mm in width, and 30 mm in height (not drawn). These dimensions yield a resonance frequency of approximately 5 GHz for the TE101 eigenmode.

Figure 1(e) displays an optical image of the lower part of the device chip. Because of space limitations, the upper part of the chip, which extends all the way to the upper sidewall of the cavity, is not shown. The chip substrate is high-resistivity silicon. The long strip, false-colored blue, is a 100-nm-thick Nb superconducting film that serves as the antenna for coupling the device and the cavity modes. The width (w) of the antenna is ~ 0.2 mm. One end of the antenna is inserted into the cavity with a length of $L \sim 2.45$ mm. The other end of the antenna is located inside the recess and is connected to one electrode of an InAs-Al device.

Figures 1(f)–1(h) show the optical image and scanning electron micrographs (SEMs). The InAs-Al wire was grown via molecular beam epitaxy [48]. Quantized zero-bias conductance peaks and peak-to-dip transitions have been reported in these hybrid nanowires as possible signatures of Majorana or quasi-Majorana zero modes [30,49]. For this experiment, a small segment of the Al shell was etched to form a Josephson junction. The two contacting electrodes are Ti/Nb (1 nm/100 nm) with one connected to the antenna and the other connected to a shorter Nb strip [length 0.3 mm; see Fig. 1(f)]. The InAs-Al Josephson junction, its electrodes, and the antenna together constitute a superconducting transmon qubit [50]. As the Josephson coupling E_J can be tuned by a side gate, this type of qubit is also referred to as a gatemon [2]. The side gate was created in the same lithography step as the contacts. Further details on the device fabrication can be found in the Appendix.

III. FINITE-ELEMENT SIMULATION

To assess the feasibility of this 3D circuit QED architecture, we performed a finite-element simulation using the High Frequency Structure Simulator (HFSS) software; see the Appendix for a detailed description. Figure 2(a) illustrates the spatial distribution of the electric field E, corresponding to the TE101 mode of the 3D cavity without the device chip inside. The inclusion of the recess does not significantly alter the distribution of E. Figure 2(c) shows the distribution of E along the central axis of the recess [the y axis labeled in Fig. 2(a)]. Upon inserting a device chip, the superconducting antenna behaves as an electric dipole and significantly modifies the distribution of E [51,52].

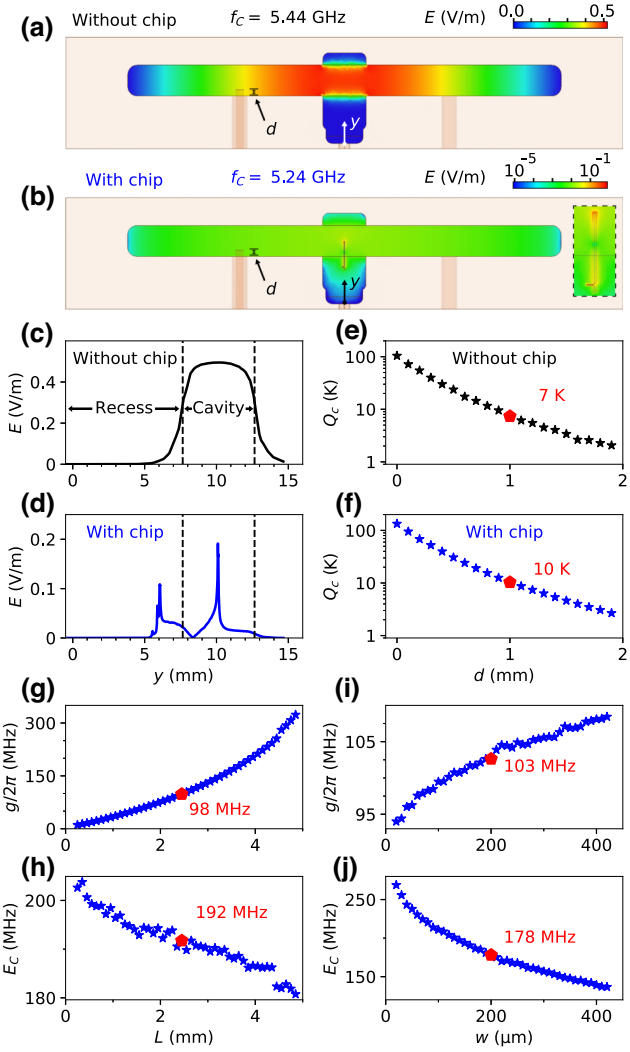

FIG. 2. Finite-element simulation. (a),(b) Electric field E distribution of the TE101 mode in the cavity (a) without and (b) with a device chip. The inset [dashed box in (b)] is an enlargement of the antenna region. (c),(d) The E distribution along the y axis for (a) and (b), respectively. (e),(f) Simulated coupling quality factor Q_c as a function of the penetration length d of the SMA pin (e) without and (f) with the device chip. (g) Qubit-cavity coupling strength g as a function of the antenna penetrating length L. (h) Charging energy E_C as a function of L. (i),(j) Plots of g and E_C as functions of the antenna width w. The red symbols in (e)–(j) correspond to the parameters of devices A, B, and C (see the Appendix for details of device fabrication).

In the simulation, we have simplified the nanowire region as a lumped inductor (20 nH). Figure 2(b) presents an overview of this distribution (TE101), while Fig. 2(d) shows a line cut along the y axis. The left peak in Fig. 2(d) corresponds to the edge of the antenna strip, where E tends to be the strongest near the sharp edges of a conductor, as shown in the inset of Fig. 2(b). The recess height is designed to be large enough to minimize the proximity effect from the antenna to the recess [the left peak in Fig. 2(d)]; see Fig. 5 in the Appendix for the simulation. For the field distributions of other microwave modes and the qubit mode, see Fig. 6 in the Appendix.

We then simulated the coupling strength between the SMA connector and the cavity mode (TE101), represented by the coupling quality factor Q_c. This factor Q_c was extracted by fitting the simulated reflection coefficient of the cavity in the driven mode, using the formula in Ref. [53]. Figure 2(e) depicts Q_c as a function of the length d of the SMA pin inserted into the cavity (without the device chip). As the SMA pin penetrates deeper into the cavity, Q_c decreases, indicating a stronger coupling between the cavity and the probe. Figure 2(f) shows a similar trend when a device chip is inserted. The red symbols in the panels of Fig. 2 correspond to the actual parameters of device A. The Q_c value of 10 K in Fig. 2(f) is slightly higher than that in Fig. 2(e) (7 K), possibly due to the presence of the chip substrate modifying the field distribution of the cavity mode. We have simulated a test case with only the device substrate (without the antenna and nanowire devices): the calculated Q_c is also around 10 K, suggesting the significant role of the substrate.

Figure 2(g) shows the qubit-cavity coupling strength, g, as a function of L, the length of the part of the antenna that is inside the cavity [see Fig. 1(e) for its labeling]. The part of the antenna located inside the recess is 1.55 mm in length and kept fixed. To extract g, we used the method of energy participation ratio to calculate the cross-Kerr coefficient, which is a function of g [54,55]; see the Appendix for details. Increasing L results in a stronger g and a smaller charging energy E_C of the qubit, as shown in Fig. 2(h). An $E_C \sim 190$ MHz (the red symbol) is typical for a gatemon qubit [9]. In Figs. 2(i) and 2(j), we varied the antenna width w and simulated the changes in g and E_C, respectively. The values of the red symbols differ slightly among Figs. 2(g), 2(h), 2(i), and 2(j), likely due to the different mesh shapes used in the finite-element analysis.

IV. CAVITY MEASUREMENT

Next, we characterize the reflection coefficient of the 3D cavity, loaded into a dilution fridge with a base temperature below 50 mK. Note that the labeling, S_{21}, refers to the vector network analyzer (VNA), while, for the cavity, S_{11} (reflection coefficient) was measured throughout this work; see Fig. 7 in the Appendix for circuit details on input and output connections. Figure 3(a) shows $|S_{21}|$ as a function of probe frequency f_r without a device chip inside the cavity. Prior to measurement, the cavity was annealed in dry air [56] to enhance its quality factor. Figure 8 in the Appendix shows its postannealing photograph [Fig. 1(a) is the one before annealing].

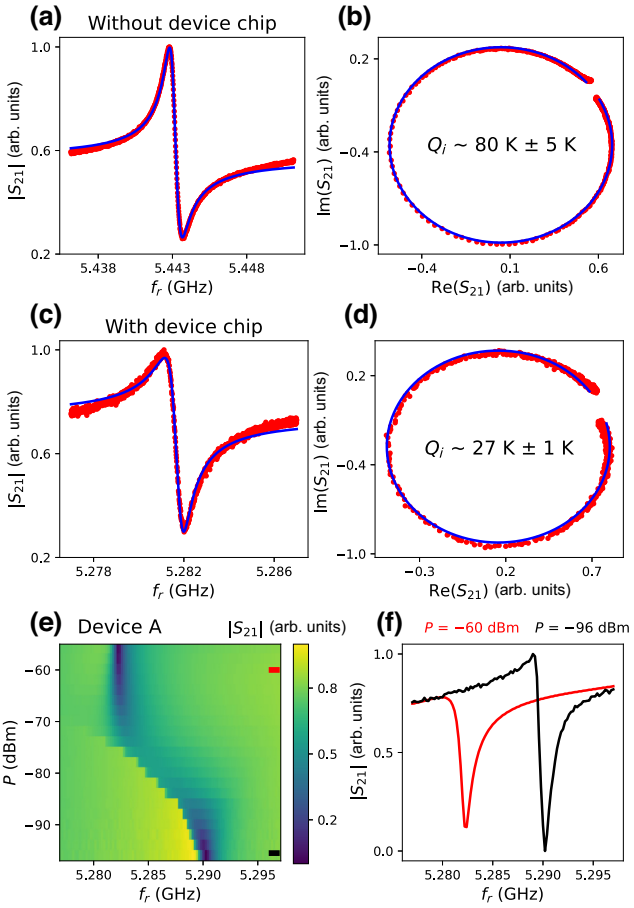

FIG. 3. Cavity reflection. (a) Plot of $|S_{21}|$ as a function of probe frequency f_r. The blue line is a fit. The cavity has no device chip inside. (b) Plot of S_{21} versus f_r in the complex plane. (c),(d) Reflection coefficient of the same cavity with a device chip (device A) inserted; $V_G = -8$ V. (e) Plot of $|S_{21}|$ versus f_r and the probe power P for device A; $V_G = 11.0$ V. (f) Line cuts from (e) at the high-power (red) and the low-power (black) regimes.

The microwave probe power at the cavity port 1 was about −96 dBm, calculated based on the VNA output power and the circuit attenuators [Fig. 7 in the Appendix]. If the losses of the microwave cables were taken into account (∼ −20 dBm attenuation at 5 GHz), the actual power at the cavity port 1 would be ∼ −120 dBm. The cavity resonant frequency is $f_C = 5.443$ GHz. The blue curve in Fig. 3(a) is fitted based on the formula [53]:

$$S_{21} = A\left[1 - 2\,\frac{(Q_l/|Q_c\cos(\theta)|)e^{i\theta}}{1 + 2iQ_l(f_r - f_C)/f_C}\right],$$

The coupling quality factor Q_c is estimated to be ~ 7360, consistent with the simulation in Fig. 2(e). The loaded (total) quality factor, $Q_l = (1/Q_i + 1/Q_c)^{-1}$, is ~ 6740. We infer the internal quality factor Q_i to be $(80 \pm 5) \times 10^3$. Figure 3(b) shows S_{21} in the complex plane where the fitting agrees reasonably well with the experimental data.

Figures 3(c) and 3(d) show the S_{21} measurement of the same cavity, but with a chip (device A) inserted. The probe power was about -96 dBm, the same as in the no-chip case. The gate voltage V_G was set to -8.0 V, pinching off the Josephson junction and making the qubit frequency far away from f_C. The fitting (blue curve) yields an internal

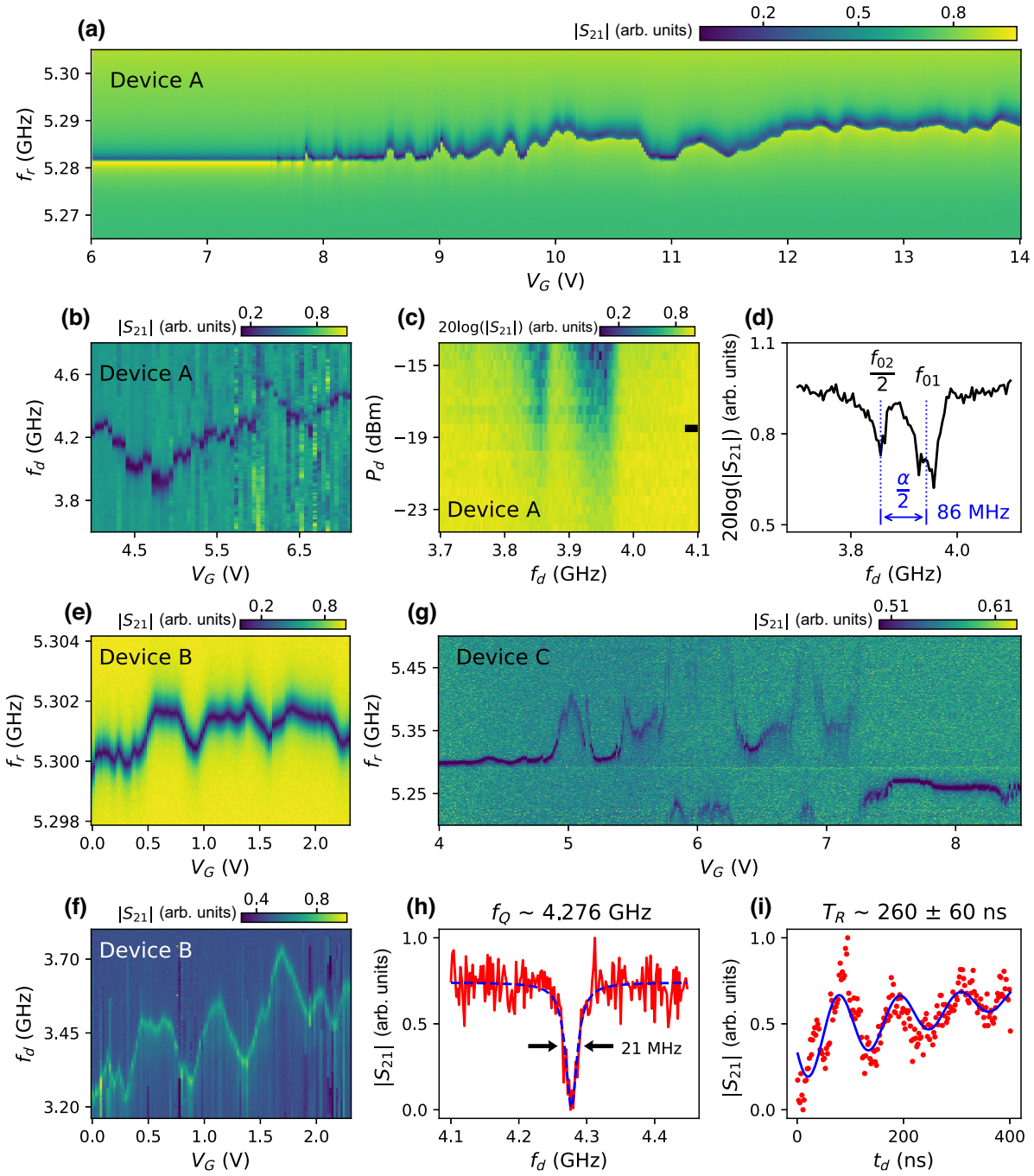

FIG. 4. Gate-tunable cavity shift and two-tone spectroscopy. (a) Gate dependence of the cavity shift of device A. (b) Two-tone spectroscopy of device A. (c) Spectroscopy as a function of qubit drive power (P_d). (d) Line cut from (c) (see the black bar), resolving the two-photon transition. (e) Gate dependence of the cavity shift of device B. (f) Two-tone spectroscopy of device B. (g) Gate dependence of the cavity shift of device C. (h) Two-tone spectroscopy of device C. The blue line is a Lorentzian fit. (i) Rabi oscillation in time-domain measurement. Gate voltage $V_G = 3.88$ V for (h) and (i).

quality factor $Q_i \sim (27 \pm 1) \times 10^3$, an acceptable value, although significantly smaller than in the no-chip case. This reduction in Q_i is attributed to the loss caused by the device chip. The resonant frequency $f_C = 5.2816$ GHz differs from that in the no-chip case by roughly 160 MHz. This difference is likely due to the redistribution of the electric field because of the device chip (and the antenna). The simulated f_C in Figs. 2(a) and 2(b) are 5.44 and 5.24 GHz, respectively, roughly consistent with the experimental data in Figs. 3(a)–3(d). The Q_c value extracted is $\sim$ 7270, slightly lower than in the simulation in Fig. 2(f). This discrepancy likely arises from minor variation of the penetration length of the SMA pin upon reloading. For the power dependence of Q_i, see Fig. 8 in the Appendix.

We then set V_G to 11.0 V to activate the Josephson element, which brought the qubit frequency close to f_C. In this regime, the interaction between the qubit and the cavity can be observed in the power (P) dependence of the cavity reflection, as shown in Fig. 3(e). The shift of the cavity resonant frequency from the high probe power regime [the red curve in Fig. 3(f)] to the lower probe power regime (the black curve) is the cavity-qubit dispersive shift. A lower Q_i of the cavity ($\sim$ 8300) is extracted due to the qubit-induced cavity relaxation (the Purcell effect) [57].

V. GATEMON MEASUREMENT

Figure 4(a) shows the gate dependence of the cavity shift for device A at the power of -86 dBm. At low V_G, the Josephson element is pinched off, and the bare cavity frequency (f_{bare}) is resolved. As V_G increases, the Josephson element is turned on, causing the cavity shift. The shift amplitude $\chi/2\pi \equiv f_C - f_{\text{bare}}$ can be calculated (in the dispersive regime) to be g^2/Δ [50], where the detuning $\Delta/2\pi = f_{\text{bare}} - f_Q$, with f_Q the qubit frequency. As $hf_Q = E_{01} \sim \sqrt{8E_J E_C}$, and $E_J(I_c)$ is a function of V_G (the critical current I_c is gate-tunable), the cavity shift is also V_G-dependent. The fluctuations in Fig. 4(a) are due to a nonmonotonic dependence of I_c on V_G, which is typical for nanowire Josephson junctions. An "anticrossing" feature is not observed for this device, suggesting that the maximum of f_Q does not exceed f_C, due to the limited gate-tunability of I_c.

We then carried out two-tone spectroscopy by fixing the readout frequency near f_C and scanning the qubit drive frequency f_d, as shown in Fig. 4(b). The dark dip denotes the qubit resonance or energy, which is V_G-dependent. The range of V_G in Fig. 4(b) does not match that in Fig. 4(a) due to the gate hysteresis; see Fig. 9 in the Appendix. The value of $g = \sqrt{\chi\Delta}$ could also be estimated from Fig. 4(b), as both f_C and f_Q can be extracted; see Fig. 10 in the Appendix for details. The estimated $g/2\pi \sim 100$ MHz is consistent with the simulation in Figs. 2(g) and 2(i).

Figure 4(c) shows the qubit spectrum as a function of the drive power P_d. A second dip at a lower energy appears; see Fig. 4(d) for a line cut. This dip is a two-photon process, corresponding to a transition from $|0\rangle$ to $|2\rangle$ (the second excited state). Its energy is thus $f_{02}/2$ while the qubit energy $f_{01} = E_{01}/h$. From the spacing of the two dips $f_{02}/2 - f_{01} = \alpha/2$, we can infer the qubit anharmonicity $\alpha = f_{12} - f_{01} \sim -172$ MHz, roughly matching the simulated charging energy (the red symbol in Fig. 2). Unlike transmons, the anharmonicity for a gatemon qubit may not be $-E_C$ but between $-E_C$ and $-E_C/4$, depending on the transmission probability of the Andreev modes in the Josephson junction [58]; see the Appendix for an estimation of this probability. Given that the Andreev modes are gate-tunable, the anharmonicity is not constant but also gate-dependent.

In Figs. 4(e) and 4(f), we show the single-tone and two-tone measurement of a second device (device B). The gate

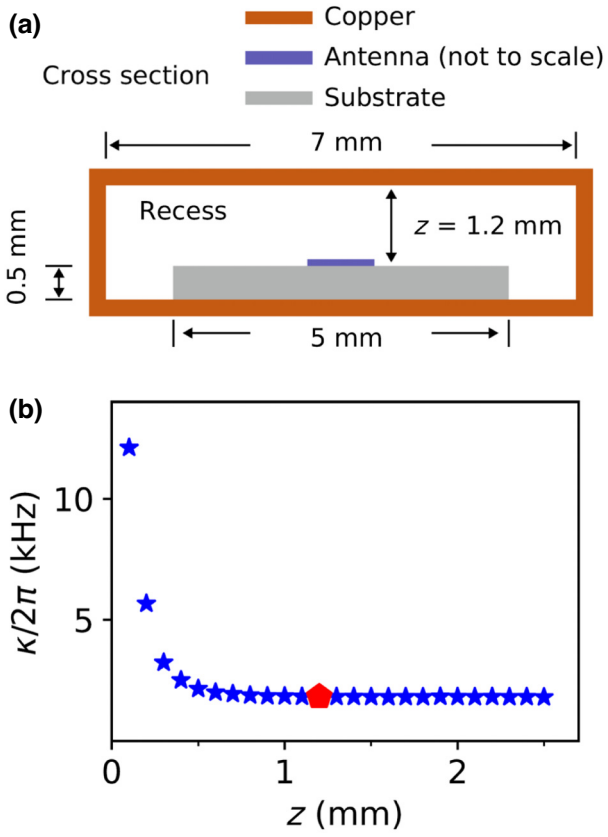

FIG. 5. (a) Schematic of the recess cross section. The antenna (100 nm thick and 0.2 mm wide) is not drawn to scale for visibility. The spacing between the antenna and the recess top wall is $z = 1.2$ mm. (b) Simulated dissipation-induced broadening of the qubit energy, $\kappa/2\pi$, as a function of z. As z approaches zero, the qubit broadening increases due to ohmic dissipation in the recess side wall. This dissipation is caused by the proximity of the qubit electric field from the antenna to the copper recess. The current design (red symbol) is in the saturated regime, suggesting that this proximity effect is not a limiting factor for the qubit coherence.

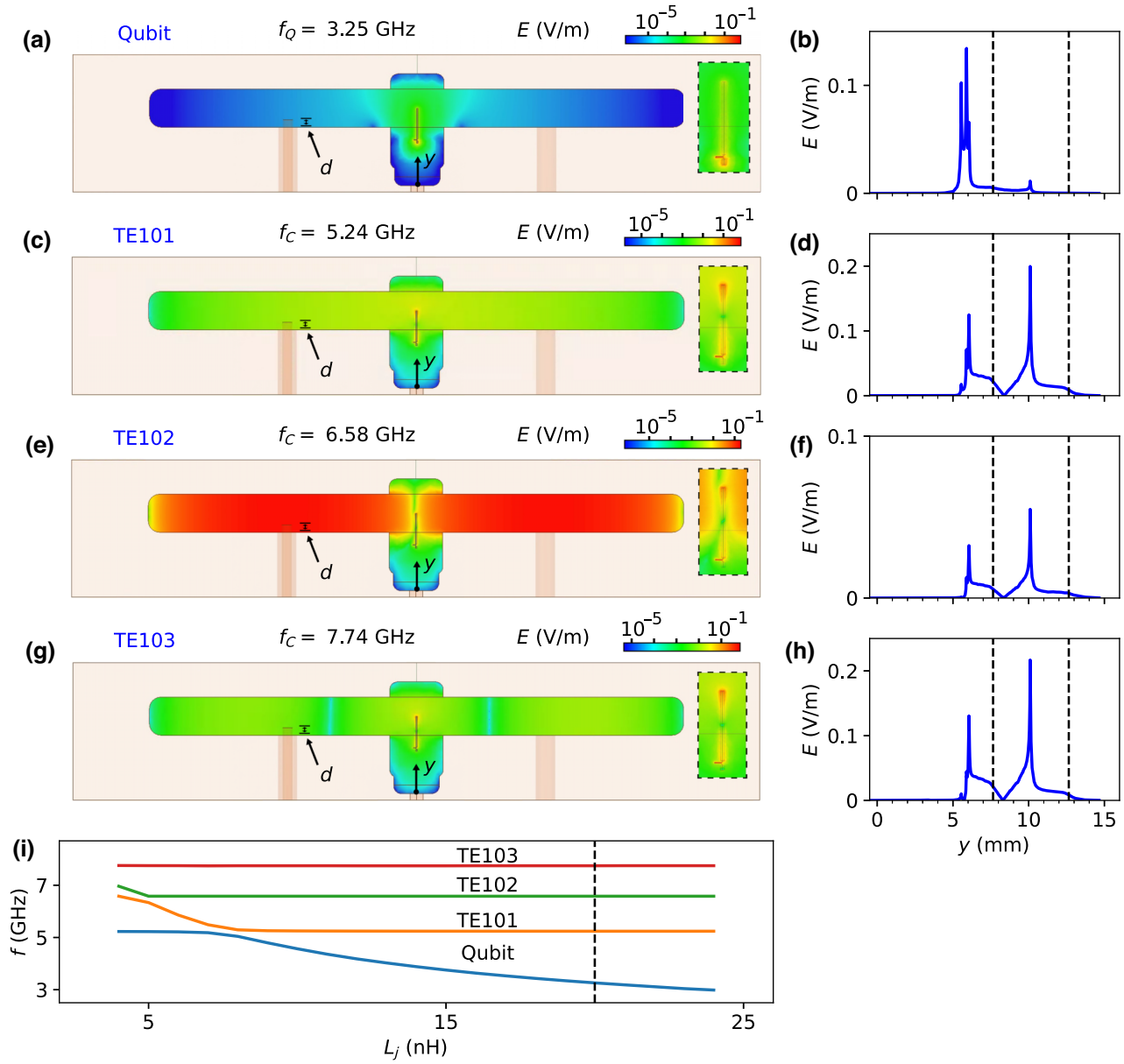

FIG. 6. Simulated electric field distribution of qubit and cavity modes. (a) Qubit mode with a frequency of 3.25 GHz. (b) Line cut along the y axis. (c),(d) TE101 mode, replotted from Figs. 2(b) and 2(d). (e),(f) TE102 and (g),(h) TE103 modes, with frequencies of 6.58 and 7.74 GHz, respectively. (i) Frequencies of the qubit mode and the three cavity modes as a function of the nanowire Josephson inductance, L_j. Only the qubit frequency varies while the cavity frequencies are constants except at the anticrossing points. The dashed line corresponds to the simulations in (a)–(h).

dependence of the qubit spectroscopy in Fig. 4(f) roughly matches with the cavity shift in Fig. 4(e). The deviations at, for example, ~ 1.2 V and 1.8 V are likely due to the mesoscopic instabilities in the device. Figure 4(g) exhibits a third device (device C), where anticrossings can be revealed, see, e.g., $V_G \sim 5.8$, 6.3 and 7 V. These anticrossings suggest that the qubit frequency can be tuned to match and exceed the cavity frequency.

We then set V_G at 3.88 V and performed the two-tone spectroscopy for device C; see the red curve in Fig. 4(h). The blue line is a Lorentzian fit of the qubit lineshape. The full width at half maximum (FWHM) is ~ 21 MHz. Figure 4(i) shows the time-domain measurement of device C by varying the duration time (t_d) of the qubit drive. Rabi oscillations were observed (red dots). The blue line is a fit using the formula $y = A\exp(-t_d/T_R)\cos(\omega t_d + B) + at_d + b$. From this fit, we extract a Rabi coherence time $T_R = 260 \pm 60$ ns. The upward slope of the background, also observed in Refs. [11,59], likely originates from the leakage to higher-level states. Further time-domain

measurements for T_1 and T_2^* are unsuccessful due to device instabilities, similar to devices A and B.

The limiting factor for further time-domain manipulation of the qubit likely lies in the quality of the device, such as contacts and gates. The superconducting film (Nb) exhibits a poor quality with a low critical temperature (T_c) of 3.9 K. This T_c is significantly lower than the typical value (∼ 9 K), possibly due to the low sputtering rate (13

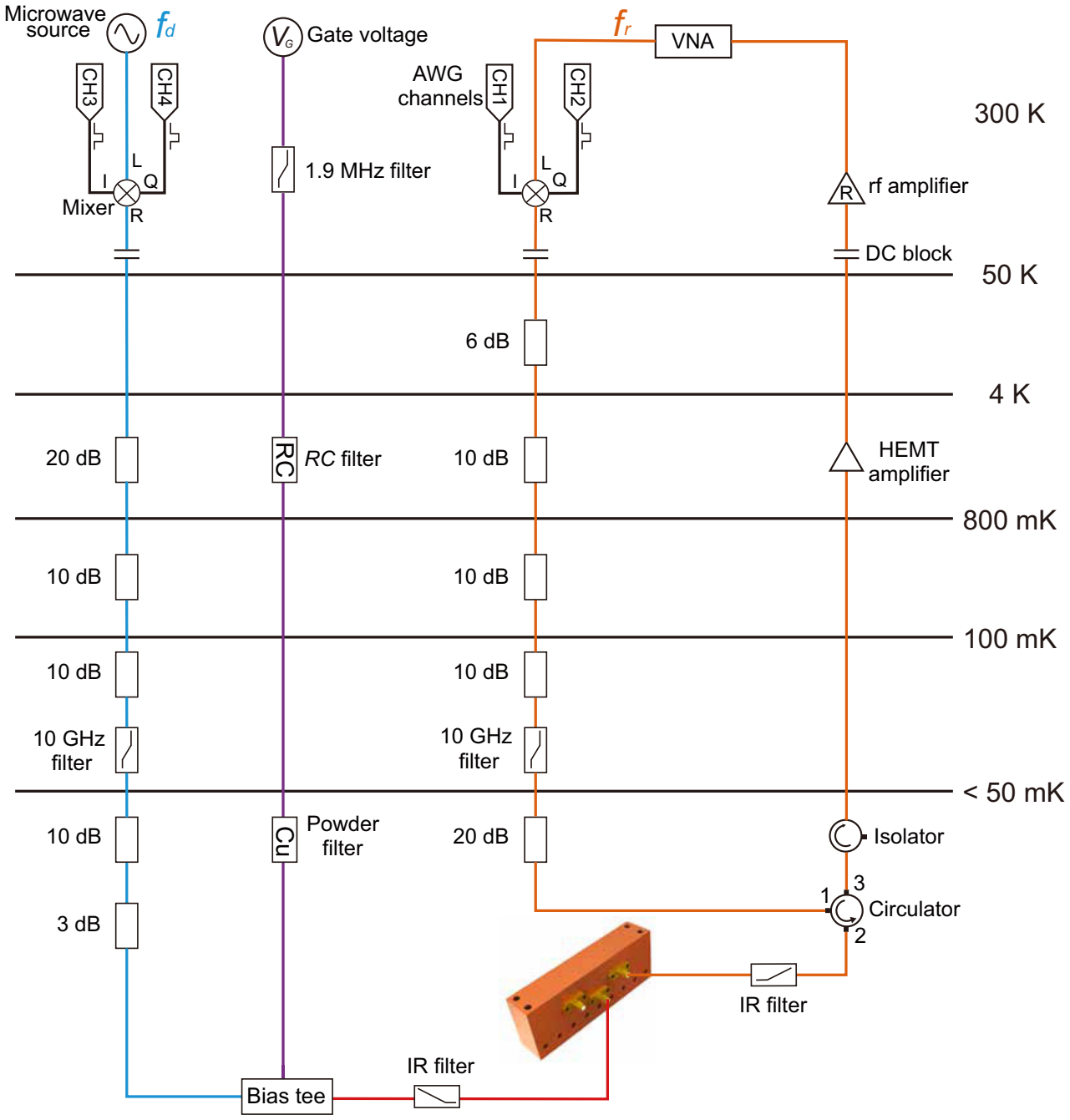

FIG. 7. Schematic of the measurement circuit. The purple line is used to apply a dc gate voltage to the device after passing through the *RC* filter and copper powder filter. The blue line is for the qubit control. A continuous microwave signal with frequency f_d was generated by the microwave source. This signal was then modulated by DRAG (derivative removal by adiabatic gate) wave pulses from an arbitrary waveform generator (AWG) through the mixer. The pulsed signal, after passing through several attenuators, was applied to the device gate line via a bias tee. The orange line is for cavity readout. A microwave signal (frequency f_r) generated by a vector network analyzer was modulated by square wave pulses and fed to the SMA port of the cavity after passing through several attenuators. The reflected signal was collected through a circulator, amplified, and then measured using the VNA.

nm/min). Future improvements on increasing this rate are necessary for higher T_c and thinner Nb films. For additional data of devices A, B and C, we refer the reader to Figs. 9 and 10 in the Appendix. In Figs. 4(b), 4(f), and 4(g), a background was subtracted to enhance visibility; see Fig. 11 in the Appendix for details. In addition to the copper cavity, we also conducted similar experiments using a 3D aluminum cavity with a similar design, and the corresponding results are presented in Fig. 12 in the Appendix.

VI. SUMMARY

In summary, we have proposed and implemented a gate-compatible 3D cavity architecture for circuit QED experiments. By incorporating an InAs-Al nanowire Josephson device into a recess machined on the sidewall of the cavity, we achieved a cavity internal quality factor of 27 000. A long superconducting strip couples the device to the cavity mode and forms a gatemon qubit with the Josephson junction. Gate-tunable cavity shift and two-tone qubit spectroscopy have been demonstrated. Our architecture allows the probing of gate-tunable quantum devices in a 3D microwave cavity. Future works could study the magnetic field compatibility, requiring thinner Nb films and higher film quality. Note that, although the copper cavity should be magnetic-field-resilient for all field directions, the device cannot survive a large perpendicular field due to vortex formation in the antenna. Other circuit designs, e.g., reducing the antenna width, are needed if a large perpendicular field is required.

Raw data and processing code within this paper are available at [60].

ACKNOWLEDGMENTS

We are grateful for valuable discussions with Luyan Sun and Christian Dickel. This work was supported by Tsinghua University Initiative Scientific Research Program, the National Natural Science Foundation of China (Grants No. 61974138, No. 92065206, No. 92065106, and No. 12374459), the Innovation Program for Quantum Science and Technology (Grant No. 2021ZD0302400) and Youth Innovation Promotion Association, Chinese Academy of Sciences (Grants No. 2017156 and No. Y2021043).

APPENDIX A: FIGURES 5–12

All the further figures mentioned in the text (i.e., Figs. 5–12) are reproduced in this appendix.

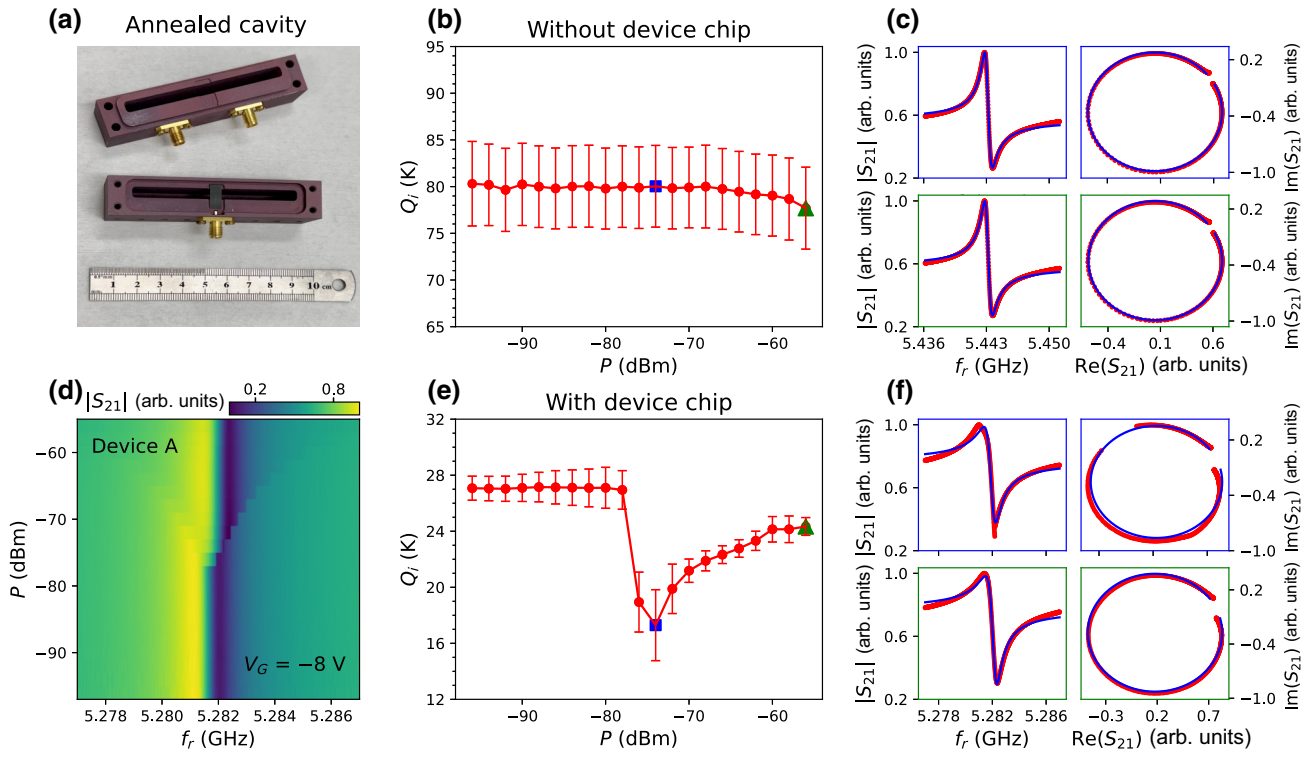

FIG. 8. (a) Postannealing photograph of the 3D cavity. (b) Power dependence of Q_i of the 3D cavity (after annealing) without the device chip inside. (c) Fitting of the cavity reflection at the power near −75 and −55 dBm, respectively. (d) Power dependence of the cavity reflection with device A inside; $V_G = -8$ V. (e) Extracted Q_i from (d). (f) Two examples of the fitting at the power near −75 and −55 dBm, respectively. The dip near −75 dBm in (e) is probably due to the Purcell effect caused by a two-level system [see panel (d)], whose origin is currently unknown.

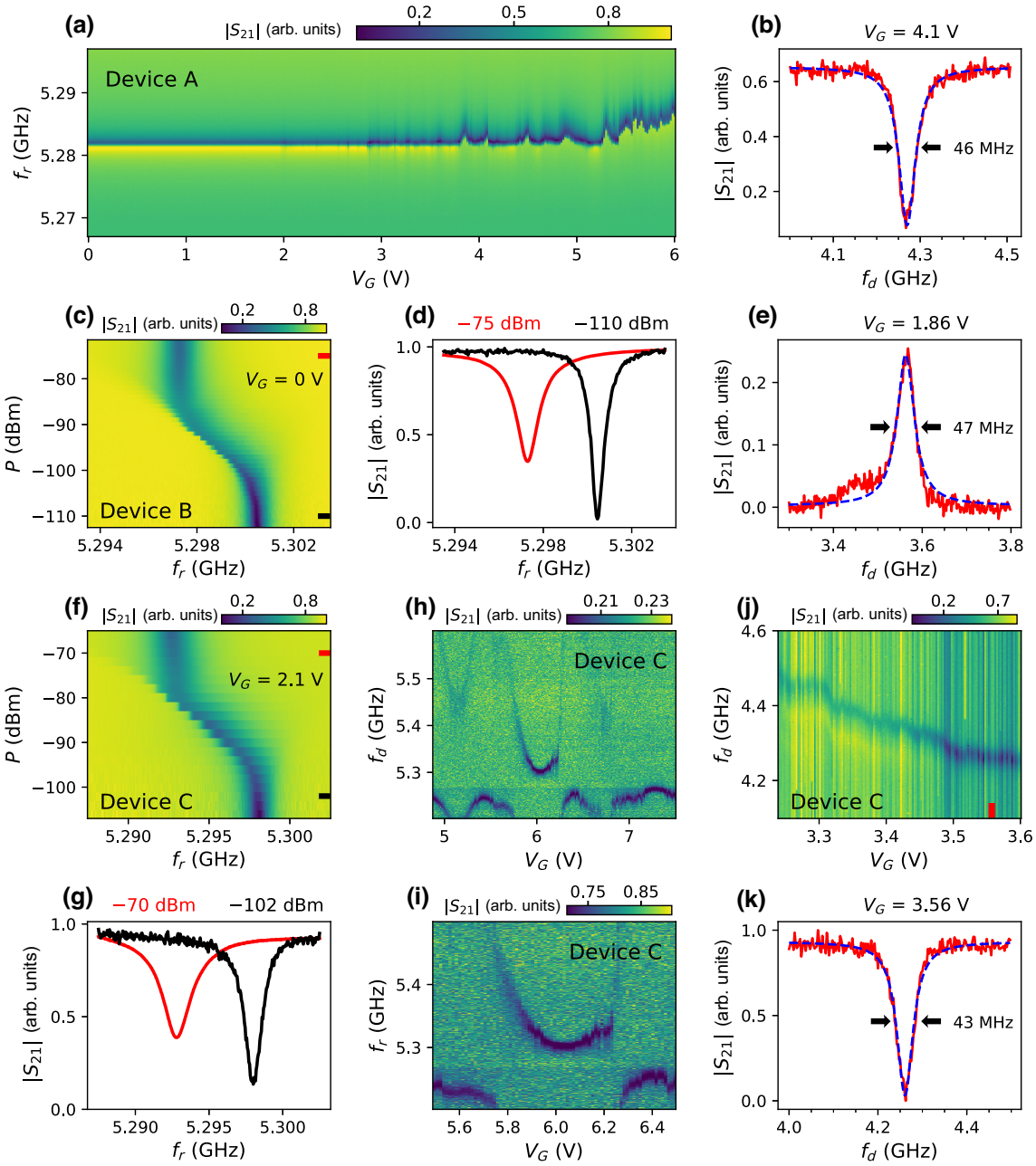

FIG. 9. (a) Gate dependence of the cavity shift of device A. The sweeping direction of V_G was from 0 to 6 V, the opposite of that in Fig. 4(a). (b) Two-tone spectroscopy, corresponding to a line cut in Fig. 4(b) at $V_G = 4.1$ V. The blue dashed line is a Lorentzian fit with a FWHM of 46 MHz. (c) Power dependence of the cavity reflection for device B. (d) Two line cuts of (c) at the high power (red) and low power (black) regimes, showing the cavity shift. (e) Two-tone spectroscopy of device B, corresponding to a line cut in Fig. 4(f) at $V_G = 1.86$ V. (f) Power dependence of the cavity reflection for device C. (g) Line cuts of (f). (h) Gate dependence of the cavity reflection for device C. (i) An enlargement of (h) on the anticrossing region. (j) Two-tone spectroscopy of device C. (k) A line cut from (j) with a FWHM of 43 MHz.

APPENDIX B: DEVICE FABRICATION AND SIMULATION

1. Antenna fabrication

A 100-nm-thick Nb superconducting film was first sputtered onto a high-resistance silicon substrate. The sputtering pressure was 5 mTorr in an argon environment. The photoresist, S1813, was spun onto the Nb film (3000 rpm, 60 s) and baked at 115°C for 120 s. Then direct laser writing was used to define the patterns for the antenna, markers, and gate line. After developing in MF319 for 1 min, reaction ion etching (O_2 pressure 5 Pa, 50 W for

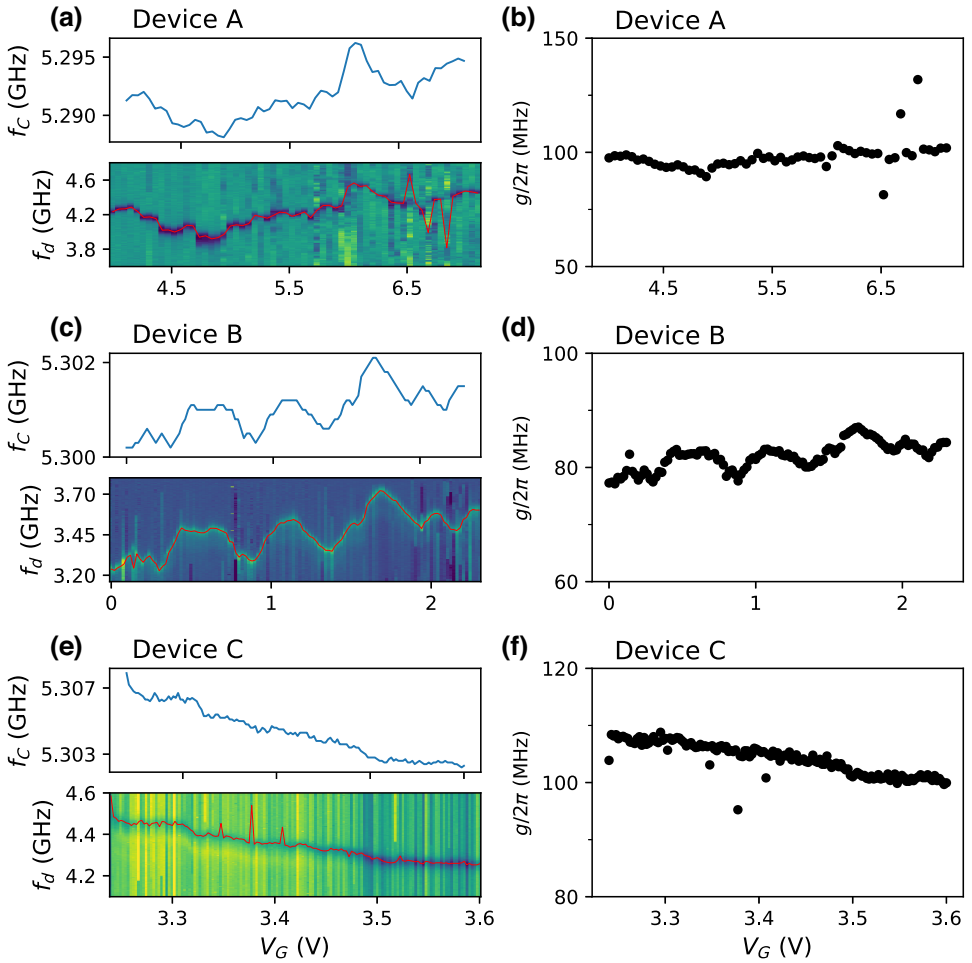

FIG. 10. Estimation of g. (a) Upper panel is the cavity resonant frequency f_C as a function of V_G for device A. Lower panel is the corresponding two-tone measurement [Fig. 4(b)], with the red line highlighting the qubit frequency f_Q. The actual measurement sequence was as follows: At each fixed V_G, before scanning the two-tone (qubit drive), the cavity drive was scanned first to extract f_C. We then calculate the dispersive shift $\chi/2\pi = f_C - f_{\text{bare}}$, and the detuning $\Delta/2\pi = f_{\text{bare}} - f_Q$. (b) Then $g = \sqrt{\chi\Delta}$ can be estimated, as shown. The value $g \sim 100$ MHz is consistent with the simulation in Figs. 2(g) and 2(i). (c)–(f) Similar estimations for devices B and C. The g value for device B (~ 80 MHz) is slightly lower than the simulation, possibly due to the inaccurate placement of the chip.

20 s; CF_4 pressure 2 Pa, 100 W for 165 s) was performed to etch away the Nb film region uncovered by the resist. Finally, the residual resist was dissolved in acetone.

2. Nanowire device fabrication

Thin InAs nanowires were grown by molecular beam epitaxy, followed by an in-situ deposition of an Al film (half shell, 15 nm thick). These hybrid wires were then transferred, through wiping of clean room tissues, from the growth chip onto the Si substrate where an antenna has been fabricated. Poly(methyl methacrylate) PMMA 672.045 (A4.5) resist was then spun at 4000 rpm for 1 min and baked at 120°C for 10 min. Electron beam lithography (EBL) was performed to pattern the etch windows. After development in methyl isobutyl ketone plus isopropyl alcohol MIBK:IPA = 1:3 for 50 s and postbaking at 130°C for 3 min, the chip was immersed in Transene Aluminum Etchant Type D at 50°C for 10 s. After the wet etching, the resist was removed in acetone. Another EBL (resist PMMA 671.05) was then performed for the contacts and side gate electrodes by sputtering Ti and Nb (thickness 1 nm and 100 nm) for devices B and C; for device A, it was Ti/NbN (1 nm/100 nm); for device D, it was Ti/NbTiN (1 nm/100 nm). Before the sputtering, a short argon plasma etching (90 s, 50 W, 0.05 Torr) was performed in-situ to ensure good ohmic contact.

3. Finite-element simulation

To solve the eigenmode, the copper conductivity of the cavity was assumed to be 1.5×10^{10} $(\Omega\ \text{m})^{-1}$. The SMA pin was assigned to be copper beryllium alloy of conductivity 1.55×10^7 $(\Omega\ \text{m})^{-1}$ from the database. The dielectric constant of the substrate (Si) was set to be 11.9 with a dielectric loss tangent of 1.5×10^{-7}.

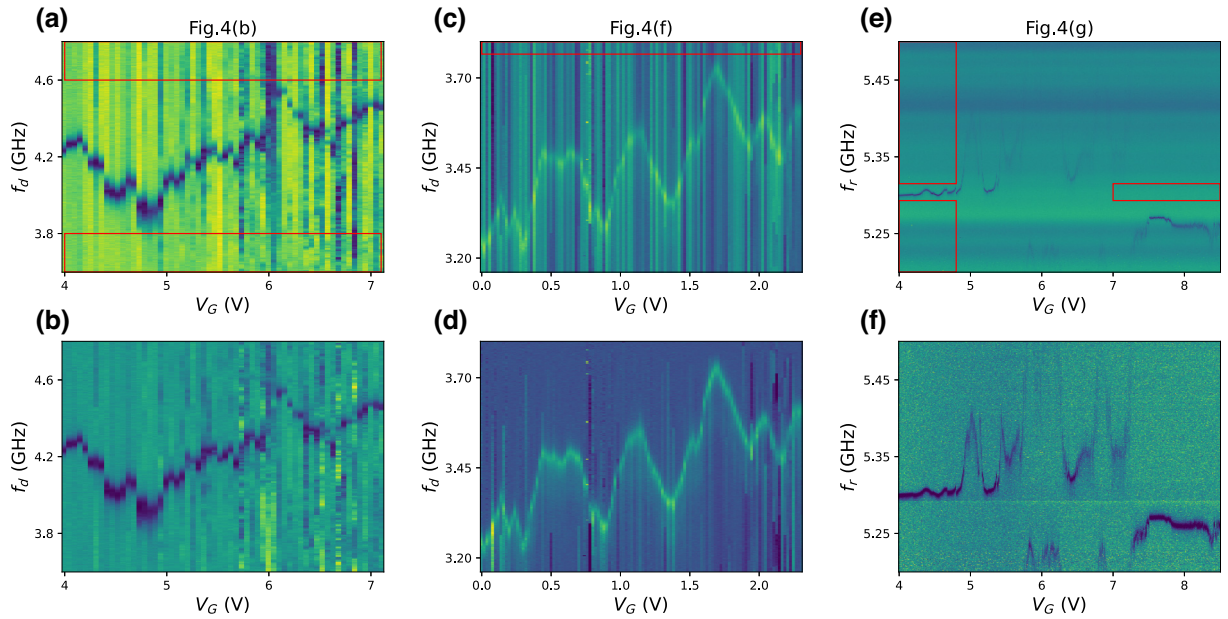

FIG. 11. Background subtraction. (a),(c),(e) The raw data corresponding to Figs. 4(b), 4(f) and 4(g); (b),(d),(f) the corresponding data after background subtraction. For (a) and (c), the signal within the red boxes was averaged for each value of V_G as the background. The background was then subtracted from the raw data. For panel (e) the average was along the V_G axis (another direction) within the red boxes.

We assumed the antenna film as a 2D conductor with a perfect electrical boundary, i.e., E is perpendicular to its surface (a perfect conductor). We made this assumption because the resistance of a superconducting film is negligible, and the thickness of 100 nm is thin enough compared to the antenna size and the wavelength of microwaves. The InAs-Al Josephson junction was simplified as an inductor with an inductance of 20 nH, as the nanowire in a gatemon is a Josephson junction, which can be treated as an inductor to the first-order approximation.

The geometric size of the contacts near the device was enlarged to be compatible with the mesh size and to reduce computational cost. The Q_c value was extracted by fitting the simulated reflection coefficient near the cavity resonant frequency. To calculate the qubit parameters, the rounded corners of the cavity were assumed to have rectangular shapes in the model and the cavity was set to be a perfect conductor. The E_C value was extracted from the calculated qubit frequency $hf_Q = \sqrt{8E_J E_C}$.

HFSS simulations typically do not provide direct information about g. To extract g, we used the method of energy participation ratio (EPR) to calculate the cross-Kerr coefficient via the Python module pyEPR (pyEPR-quantum), following Ref. [54] (the cross-Kerr coefficient is a function of g). We first expand and separate the Josephson energy term $(-E_J \cos\varphi_J)$ in the Hamiltonian into linear and nonlinear parts: $H = H_{\text{lin}} + H_{\text{nl}} = \hbar\omega_C a_C^\dagger a_C + \hbar\omega_Q a_Q^\dagger a_Q - E_J[1 + \frac{1}{24}\varphi_J^4 - \frac{1}{720}\varphi_J^6 + \cdots]$, where $\varphi_J = \varphi_C(a_C^\dagger + a_C) + \varphi_Q(a_Q^\dagger + a_Q)$. Here φ_C and φ_Q are the quantum zero-field fluctuations of the junction flux in the cavity and qubit mode, respectively.

We then calculate the EPR (p_m) of the junction in the mode m (m = cavity or qubit), defined to be the fraction of inductive energy stored in the junction relative to the total inductive energy stored in the entire circuit. The p_m value is proportional to φ_C^2 and φ_Q^2, and can also be calculated using the electromagnetic (EM) field distribution by definition. Note that the total electrical energy and total inductive energy of a resonant system are equal. Thus, we can calculate the quantum Hamiltonian based on the classical EM field. From $p_m = \langle\psi_m|\,\frac{1}{2}E_J\varphi_J^2\,|\psi_m\rangle / \langle\psi_m|\,\frac{1}{2}H_{\text{lin}}\,|\psi_m\rangle$, we can get $\varphi_C^2 = p_C\hbar\omega_C/2E_J$ and $\varphi_Q^2 = p_Q\hbar\omega_Q/2E_J$. We can simulate

$$p_m = \frac{E_{jj}}{E_{\text{ind-of-tot}}} = \frac{E_{\text{ind-of-tot}} - E_{\text{ind-of-field}}}{E_{\text{ind-of-tot}}} = \frac{E_{\text{cap-of-field}} - E_{\text{ind-of-field}}}{E_{\text{cap-of-field}}}.$$

We can then get the cross-Kerr coefficient

$$\chi_{QC} = -2\,\frac{g^2 E_C/\hbar}{(\omega_Q - \omega_C)(\omega_Q - \omega_C - E_C/\hbar)},$$

from which g can be estimated.

4. Estimation of the Josephson junction transparency

The anharmonicity $\alpha = -E_C(1 - (3\sum T_i^2/4\sum T_i))$, where T_i is the transparency of the ith occupied Andreev mode. For simplicity, we assume N modes with equal

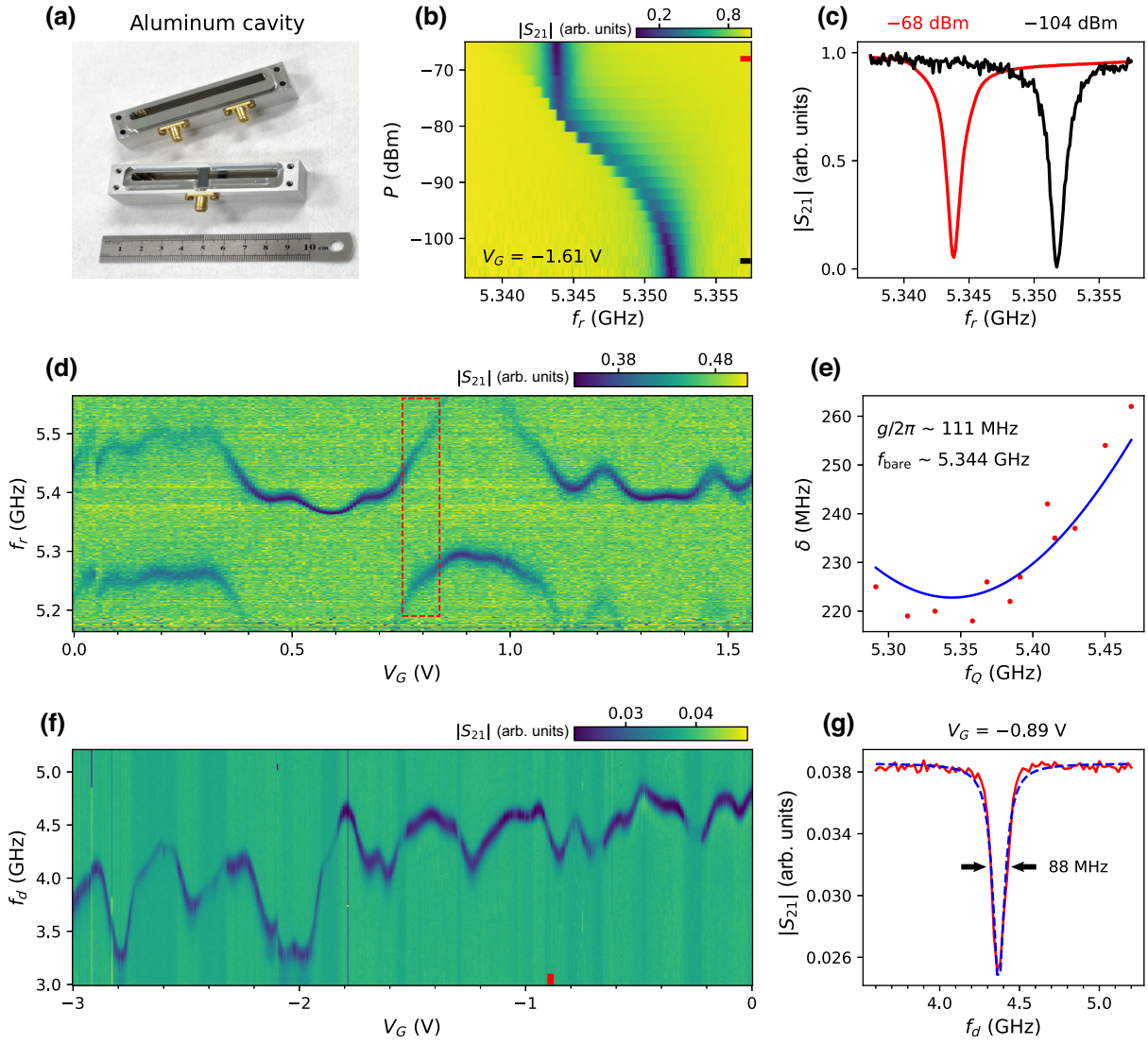

FIG. 12. Gatemon qubit in a 3D aluminum cavity. (a) Photograph of the 3D Al cavity with a device chip (device D). (b) Power dependence of the cavity shift. The reflection coefficient of the cavity was measured. (c) Line cuts from (b) at the high power (red) and low power (black) regimes. (d) Gate dependence of the cavity shift with clear anticrossings. (e) The spacing $\delta = f_+ - f_-$ between the anticrossing dips as a function of the qubit frequency ($f_Q = f_+ + f_- - f_{\text{bare}}$), where f_+ and f_- are the frequencies of the two dips within the red box in (d). The blue line is a fit based on the formula $\delta = \sqrt{(f_Q - f_{\text{bare}})^2 + 4(g/2\pi)^2}$, where $g/2\pi$ of 111 MHz can be extracted. (f) Two-tone qubit spectroscopy. (g) A line cut from (f) at $V_G = -0.89$ V. The blue dashed line is a Lorentzian fit.

transparency $T = \sum T_i/N$. In Fig. 4(d), $\alpha \sim -172$ MHz. From the simulation, we get $E_C \sim 178$–192 MHz (we take the average 185 MHz), so $E_J = (hf_Q)^2/8E_C \sim 10$ GHz. But also $E_J = (\Delta/4)\sum T_i$, where Δ is the superconducting gap, here ~ 300 μeV (75 GHz) based on our transport measurement. Therefore, $\sum T_i \sim 0.533$. So from $\alpha = -E_C(1 - (3\sum T_i/4N))$, we get $N \sim 6$ and $T \sim 0.09$.

[1] F. Arute, K. Arya, R. Babbush, D. Bacon, J. Bardin, R. Barends, R. Biswas, S. Boixo, F. Brandao, D. Buell, *et al.*, Quantum supremacy using a programmable superconducting processor, Nature **574**, 505 (2019).

[2] T. W. Larsen, K. D. Petersson, F. Kuemmeth, T. S. Jespersen, P. Krogstrup, J. Nygård, and C. M. Marcus, Semiconductor-Nanowire-Based Superconducting Qubit, Phys. Rev. Lett. **115**, 127001 (2015).

[3] G. de Lange, B. van Heck, A. Bruno, D. J. van Woerkom, A. Geresdi, S. R. Plissard, E. P. A. M. Bakkers, A. R. Akhmerov, and L. DiCarlo, Realization of Microwave Quantum Circuits Using Hybrid Superconducting-Semiconducting Nanowire Josephson Elements, Phys. Rev. Lett. **115**, 127002 (2015).

[4] L. Casparis, T. W. Larsen, M. S. Olsen, F. Kuemmeth, P. Krogstrup, J. Nygård, K. D. Petersson, and C. M. Marcus, Gatemon Benchmarking and Two-Qubit Operations, Phys. Rev. Lett. **116**, 150505 (2016).

[5] F. Luthi, T. Stavenga, O. W. Enzing, A. Bruno, C. Dickel, N. K. Langford, M. A. Rol, T. S. Jespersen, J. Nygård, P. Krogstrup, and L. DiCarlo, Evolution of Nanowire Transmon Qubits and Their Coherence in a Magnetic Field, Phys. Rev. Lett. **120**, 100502 (2018).

[6] L. Casparis, M. Connolly, M. Kjaergaard, N. Pearson, A. Kringhøj, T. Larsen, F. Kuemmeth, T. Wang, C. Thomas, S. Gronin, G. Gardner, M. Manfra, and C. Marcus, Superconducting gatemon qubit based on a proximitized two-dimensional electron gas, Nat. Nanotechnol. **13**, 915 (2018).

[7] J. I.-J. Wang, D. Rodan-Legrain, L. Bretheau, D. L. Campbell, B. Kannan, D. K. Kim, M. Kjaergaard, P. Krantz, G. O. Samach, F. Yan, J. L. Yoder, K. Watanabe, T. Taniguchi, T. P. Orlando, S. Gustavsson, P. Jarillo-Herrero, and W. D. Oliver, Coherent control of a hybrid superconducting circuit made with graphene-based van der Waals heterostructures, Nat. Nanotechnol. **14**, 120 (2018).

[8] T. Schmitt, M. Connolly, M. Schleenvoigt, C. Liu, O. Kennedy, J. Chávez-Garcia, A. R. Jalil, B. Bennemann, S. Trellenkamp, F. Lentz, E. Neumann, T. Lindström, S. Graaf, J. Berenschot, N. Tas, G. Mussler, K. D. Petersson, D. Grützmacher, and P. Schüffelgen, Integration of topological insulator Josephson junctions in superconducting qubit circuits, Nano Lett. **22**, 2595 (2022).

[9] J. Huo, Z. Xia, Z. Li, S. Zhang, Y. Wang, D. Pan, Q. Liu, Y. Liu, Z. Wang, Y. Gao, J. Zhao, T. Li, J. Ying, R. Shang, and H. Zhang, Gatemon qubit based on a thin InAs-Al hybrid nanowire, Chin. Phys. Lett. **40**, eid 047302 (2023).

[10] R. Aguado, A perspective on semiconductor-based superconducting qubits, Appl. Phys. Lett. **117**, 240501 (2020).

[11] T. W. Larsen, M. E. Gershenson, L. Casparis, A. Kringhøj, N. J. Pearson, R. P. G. McNeil, F. Kuemmeth, P. Krogstrup, K. D. Petersson, and C. M. Marcus, Parity-Protected Superconductor-Semiconductor Qubit, Phys. Rev. Lett. **125**, 056801 (2020).

[12] M. Hays, G. de Lange, K. Serniak, D. J. van Woerkom, D. Bouman, P. Krogstrup, J. Nygård, A. Geresdi, and M. H. Devoret, Direct Microwave Measurement of Andreev-Bound-State Dynamics in a Semiconductor-Nanowire Josephson Junction, Phys. Rev. Lett. **121**, 047001 (2018).

[13] M. Hays, V. Fatemi, D. Bouman, J. Cerrillo, S. Diamond, K. Serniak, T. Connolly, P. Krogstrup, J. Nygård, A. L. Yeyati, A. Geresdi, and M. H. Devoret, Coherent manipulation of an Andreev spin qubit, Science **373**, 430 (2021).

[14] M. Pita-Vidal, A. Bargerbos, R. žitko, L. Splitthoff, L. Grünhaupt, J. Wesdorp, Y. Liu, L. Kouwenhoven, R. Aguado, B. Heck, A. Kou, and C. Andersen, Direct manipulation of a superconducting spin qubit strongly coupled to a transmon qubit, Nat. Phys. **19**, 1110 (2023).

[15] F. Schmidt, M. Jenkins, K. Watanabe, T. Taniguchi, and G. Steele, A ballistic graphene superconducting microwave circuit, Nat. Commun. **9**, 4069 (2018).

[16] J. Kroll, W. Uilhoorn, K. Enden, D. Jong, K. Watanabe, T. Taniguchi, S. Goswami, C. Cassidy, and L. Kouwenhoven, Magnetic field compatible circuit quantum electrodynamics with graphene Josephson junctions, Nat. Commun. **9**, 4615 (2018).

[17] L. Tosi, C. Metzger, M. F. Goffman, C. Urbina, H. Pothier, S. Park, A. L. Yeyati, J. Nygård, and P. Krogstrup, Spin-Orbit Splitting of Andreev States Revealed by Microwave Spectroscopy, Phys. Rev. X **9**, 011010 (2019).

[18] A. Kringhøj, B. van Heck, T. W. Larsen, O. Erlandsson, D. Sabonis, P. Krogstrup, L. Casparis, K. D. Petersson, and C. M. Marcus, Suppressed Charge Dispersion via Resonant Tunneling in a Single-Channel Transmon, Phys. Rev. Lett. **124**, 246803 (2020).

[19] A. Bargerbos, W. Uilhoorn, C.-K. Yang, P. Krogstrup, L. P. Kouwenhoven, G. de Lange, B. van Heck, and A. Kou, Observation of Vanishing Charge Dispersion of a Nearly Open Superconducting Island, Phys. Rev. Lett. **124**, 246802 (2020).

[20] D. Sabonis, O. Erlandsson, A. Kringhøj, B. van Heck, T. W. Larsen, I. Petkovic, P. Krogstrup, K. D. Petersson, and C. M. Marcus, Destructive Little-Parks Effect in a Full-Shell Nanowire-Based Transmon, Phys. Rev. Lett. **125**, 156804 (2020).

[21] M. Mergenthaler, A. Nersisyan, A. Patterson, M. Esposito, A. Baumgartner, C. Schönenberger, G. A. D. Briggs, E. A. Laird, and P. J. Leek, Circuit quantum electrodynamics with carbon-nanotube-based superconducting quantum circuits, Phys. Rev. Appl. **15**, 064050 (2021).

[22] V. Fatemi, P. D. Kurilovich, M. Hays, D. Bouman, T. Connolly, S. Diamond, N. E. Frattini, V. D. Kurilovich, P. Krogstrup, J. Nygård, A. Geresdi, L. I. Glazman, and M. H. Devoret, Microwave Susceptibility Observation of Interacting Many-Body Andreev States, Phys. Rev. Lett. **129**, 227701 (2022).

[23] F. J. Matute-Cañadas, C. Metzger, S. Park, L. Tosi, P. Krogstrup, J. Nygård, M. F. Goffman, C. Urbina, H. Pothier, and A. L. Yeyati, Signatures of Interactions in the Andreev Spectrum of Nanowire Josephson Junctions, Phys. Rev. Lett. **128**, 197702 (2022).

[24] A. Bargerbos, M. Pita-Vidal, R. Žitko, J. Ávila, L. J. Splitthoff, L. Grünhaupt, J. J. Wesdorp, C. K. Andersen, Y. Liu, L. P. Kouwenhoven, R. Aguado, A. Kou, and B. van Heck, Singlet-Doublet Transitions of a Quantum Dot Josephson Junction Detected in a Transmon Circuit, PRX Quantum **3**, 030311 (2022).

[25] R. M. Lutchyn, J. D. Sau, and S. Das Sarma, Majorana Fermions and a Topological Phase Transition in Semiconductor-Superconductor Heterostructures, Phys. Rev. Lett. **105**, 077001 (2010).

[26] Y. Oreg, G. Refael, and F. von Oppen, Helical Liquids and Majorana Bound States in Quantum Wires, Phys. Rev. Lett. **105**, 177002 (2010).

[27] V. Mourik, K. Zuo, S. M. Frolov, S. Plissard, E. P. Bakkers, and L. P. Kouwenhoven, Signatures of Majorana fermions in hybrid superconductor-semiconductor nanowire devices, Science **336**, 1003 (2012).

[28] M. Deng, S. Vaitiekėnas, E. B. Hansen, J. Danon, M. Leijnse, K. Flensberg, J. Nygård, P. Krogstrup, and C. M. Marcus, Majorana bound state in a coupled quantum-dot hybrid-nanowire system, Science **354**, 1557 (2016).

[29] Ö. Gül, H. Zhang, J. D. Bommer, M. W. de Moor, D. Car, S. R. Plissard, E. P. Bakkers, A. Geresdi, K. Watanabe, T. Taniguchi, *et al.*, Ballistic Majorana nanowire devices, Nat. Nanotechnol. **13**, 192 (2018).

[30] Z. Wang, H. Song, D. Pan, Z. Zhang, W. Miao, R. Li, Z. Cao, G. Zhang, L. Liu, L. Wen, R. Zhuo, D. E. Liu, K. He, R. Shang, J. Zhao, and H. Zhang, Plateau Regions for Zero-Bias Peaks Within 5% of the Quantized Conductance Value $2e^2/h$, Phys. Rev. Lett. **129**, 167702 (2022).

[31] E. Ginossar and E. Grosfeld, Microwave transitions as a signature of coherent parity mixing effects in the Majorana-transmon qubit, Nat. Commun. **5**, 4772 (2014).

[32] S. Plugge, A. Rasmussen, R. Egger, and K. Flensberg, Majorana box qubits, New J. Phys. **19**, 012001 (2017).

[33] M. C. Dartiailh, T. Kontos, B. Douçot, and A. Cottet, Direct Cavity Detection of Majorana Pairs, Phys. Rev. Lett. **118**, 126803 (2017).

[34] A. Keselman, C. Murthy, B. van Heck, and B. Bauer, Spectral response of Josephson junctions with low-energy quasiparticles, SciPost Phys. **7**, 050 (2019).

[35] A. Wallraff, D. Schuster, A. Blais, L. Frunzio, R. Huang, J. Majer, S. Kumar, S. Girvin, and R. Schoelkopf, Strong coupling of a single photon to a superconducting qubit using circuit quantum electrodynamics, Nature **431**, 162 (2004).

[36] N. Samkharadze, A. Bruno, P. Scarlino, G. Zheng, D. P. DiVincenzo, L. DiCarlo, and L. M. K. Vandersypen, High-kinetic-inductance superconducting nanowire resonators for circuit QED in a magnetic field, Phys. Rev. Appl. **5**, 044004 (2016).

[37] J. Kroll, F. Borsoi, K. van der Enden, W. Uilhoorn, D. de Jong, M. Quintero-Pérez, D. van Woerkom, A. Bruno, S. Plissard, D. Car, E. Bakkers, M. Cassidy, and L. Kouwenhoven, Magnetic-field-resilient superconducting coplanar-waveguide resonators for hybrid circuit quantum electrodynamics experiments, Phys. Rev. Appl. **11**, 064053 (2019).

[38] M. Pita-Vidal, A. Bargerbos, C.-K. Yang, D. J. van Woerkom, W. Pfaff, N. Haider, P. Krogstrup, L. P. Kouwenhoven, G. de Lange, and A. Kou, Gate-tunable field-compatible fluxonium, Phys. Rev. Appl. **14**, 064038 (2020).

[39] A. Kringhøj, T. W. Larsen, O. Erlandsson, W. Uilhoorn, J. Kroll, M. Hesselberg, R. McNeil, P. Krogstrup, L. Casparis, C. Marcus, and K. Petersson, Magnetic-field-compatible superconducting transmon qubit, Phys. Rev. Appl. **15**, 054001 (2021).

[40] H. Paik, D. I. Schuster, L. S. Bishop, G. Kirchmair, G. Catelani, A. P. Sears, B. R. Johnson, M. J. Reagor, L. Frunzio, L. I. Glazman, S. M. Girvin, M. H. Devoret, and R. J. Schoelkopf, Observation of High Coherence in Josephson Junction Qubits Measured in a Three-Dimensional Circuit QED Architecture, Phys. Rev. Lett. **107**, 240501 (2011).

[41] M. Stammeier, S. Garcia, and A. Wallraff, Applying electric and magnetic field bias in a 3D superconducting waveguide cavity with high quality factor, Quantum Sci. Technol. **3**, 045007 (2018).

[42] M. A. Cohen, M. Yuan, B. W. A. de Jong, E. Beukers, S. J. Bosman, and G. A. Steele, A split-cavity design for the incorporation of a DC bias in a 3D microwave cavity, Appl. Phys. Lett. **110**, 172601 (2017).

[43] W.-C. Kong, G.-W. Deng, S.-X. Li, H.-O. Li, G. Cao, M. Xiao, and G.-P. Guo, Introduction of DC line structures into a superconducting microwave 3D cavity, Rev. Sci. Instrum. **86**, 023108 (2015).

[44] J. Krause, C. Dickel, E. Vaal, M. Vielmetter, J. Feng, R. Bounds, G. Catelani, J. M. Fink, and Y. Ando, Magnetic field resilience of three-dimensional transmons with thin-film Al/AlO_x/Al Josephson junctions approaching 1 T, Phys. Rev. Appl. **17**, 034032 (2022).

[45] L. V. Abdurakhimov, I. Mahboob, H. Toida, K. Kakuyanagi, and S. Saito, A long-lived capacitively shunted flux qubit embedded in a 3D cavity, Appl. Phys. Lett. **115**, 262601 (2019).

[46] S. Majumder, T. Bera, R. Suresh, and V. Singh, A fast tunable 3D-transmon architecture for superconducting qubit-based hybrid devices, J. Low Temp. Phys. **207**, 210 (2022).

[47] C. Rigetti, J. M. Gambetta, S. Poletto, B. L. T. Plourde, J. M. Chow, A. D. Córcoles, J. A. Smolin, S. T. Merkel, J. R. Rozen, G. A. Keefe, M. B. Rothwell, M. B. Ketchen, and M. Steffen, Superconducting qubit in a waveguide cavity with a coherence time approaching 0.1 ms, Phys. Rev. B **86**, 100506 (2012).

[48] D. Pan, H. Song, S. Zhang, L. Liu, L. Wen, D. Liao, R. Zhuo, Z. Wang, Z. Zhang, S. Yang, J. Ying, W. Miao, R. Shang, H. Zhang, and J. Zhao, In situ epitaxy of pure phase ultra-thin InAs-Al nanowires for quantum devices, Chin. Phys. Lett. **39**, eid 058101 (2022).

[49] H. Song, Z. Zhang, D. Pan, D. Liu, Z. Wang, Z. Cao, L. Liu, L. Wen, D. Liao, R. Zhuo, D. E. Liu, R. Shang, J. Zhao, and H. Zhang, Large zero bias peaks and dips in a four-terminal thin InAs-Al nanowire device, Phys. Rev. Res. **4**, 033235 (2022).

[50] J. Koch, T. M. Yu, J. Gambetta, A. A. Houck, D. I. Schuster, J. Majer, A. Blais, M. H. Devoret, S. M. Girvin, and R. J. Schoelkopf, Charge-insensitive qubit design derived from the Cooper pair box, Phys. Rev. A **76**, 042319 (2007).

[51] H. M. Doeleman, E. Verhagen, and A. F. Koenderink, Antenna–cavity hybrids: Matching polar opposites for Purcell enhancements at any linewidth, ACS Photonics **3**, 1943 (2016).

[52] I. M. Palstra, H. M. Doeleman, and A. F. Koenderink, Hybrid cavity-antenna systems for quantum optics outside the cryostat?, Nanophotonics **8**, 1513 (2019).

[53] Q.-M. Chen, M. Pfeiffer, M. Partanen, F. Fesquet, K. E. Honasoge, F. Kronowetter, Y. Nojiri, M. Renger, K. G. Fedorov, A. Marx, F. Deppe, and R. Gross, Scattering coefficients of superconducting microwave resonators. I. Transfer matrix approach, Phys. Rev. B **106**, 214505 (2022).

[54] Z. Minev, Z. Leghtas, S. Mundhada, L. Christakis, I. Pop, and M. Devoret, Energy-participation quantization of Josephson circuits, npj Quantum Inf. **7**, 131 (2021).

[55] A. Blais, A. L. Grimsmo, S. M. Girvin, and A. Wallraff, Circuit quantum electrodynamics, Rev. Mod. Phys. **93**, 025005 (2021).

[56] S. Rosenblum, W. Steyert, and F. Fickett, A simple method for producing high conductivity copper for low temperature applications, Cryogenics **17**, 645 (1977).

[57] E. M. Purcell, H. C. Torrey, and R. V. Pound, Resonance absorption by nuclear magnetic moments in a solid, Phys. Rev. **69**, 37 (1946).

[58] A. Kringhøj, L. Casparis, M. Hell, T. W. Larsen, F. Kuemmeth, M. Leijnse, K. Flensberg, P. Krogstrup, J. Nygård, K. D. Petersson, and C. M. Marcus, Anharmonicity of a superconducting qubit with a few-mode Josephson junction, Phys. Rev. B **97**, 060508 (2018).

[59] A. Hertel, M. Eichinger, L. O. Andersen, D. M. van Zanten, S. Kallatt, P. Scarlino, A. Kringhøj, J. M. Chavez-Garcia, G. C. Gardner, S. Gronin, M. J. Manfra, A. Gyenis, M. Kjaergaard, C. M. Marcus, and K. D. Petersson, Gate-tunable transmon using selective-area-grown superconductor-semiconductor hybrid structures on silicon, Phys. Rev. Appl. **18**, 034042 (2022).

[60] https://doi.org/10.5281/zenodo.10703169.